Monthly Notices
of the
ROYAL ASTRONOMICAL SOCIETY

Mon. Not. R. Astron. Soc. (2012) doi:10.1111/j.1365-2966.2012.20448.x

99 Herculis: host to a circumbinary polar-ring debris disc

G. M. Kennedy,[1⋆] M. C. Wyatt,[1] B. Sibthorpe,[2] G. Duchêne,[3,4] P. Kalas,[3] B. C. Matthews,[5,6] J. S. Greaves,[7] K. Y. L. Su[8] and M. P. Fitzgerald[9,10]

[1]*Institute of Astronomy, University of Cambridge, Madingley Road, Cambridge CB3 0HA*
[2]*UK Astronomy Technology Center, Royal Observatory, Blackford Hill, Edinburgh EH9 3HJ*
[3]*Department of Astronomy, University of California, B-20 Hearst Field Annex, Berkeley, CA 94720-3411, USA*
[4]*Laboratoire d'Astrophysique de Grenoble, CNRS/Université Joseph-Fourier (UMR 5571), BP 53, F-38041 Grenoble cedex 9, France*
[5]*Herzberg Institute of Astrophysics, National Research Council Canada, 5071 West Saanich Road, Victoria, BC V9E 2E7, Canada*
[6]*Department of Physics and Astronomy, University of Victoria, Finnerty Road, Victoria, BC V8W 3P6, Canada*
[7]*School of Physics and Astronomy, University of St Andrews, North Haugh, St Andrews, Fife KY16 9SS*
[8]*Steward Observatory, University of Arizona, 933 North Cherry Avenue, Tucson, AZ 85721, USA*
[9]*Institute of Geophysics and Planetary Physics, Lawrence Livermore National Laboratory, L-413, 7000 East Avenue, Livermore, CA 94550, USA*
[10]*Department of Physics and Astronomy, UCLA, Los Angeles, CA 90095-1547, USA*

Accepted 2011 December 29. Received 2011 December 23; in original form 2011 November 10

ABSTRACT

We present resolved *Herschel* images of a circumbinary debris disc in the 99 Herculis system. The primary is a late F-type star. The binary orbit is well characterized and we conclude that the disc is misaligned with the binary plane. Two different models can explain the observed structure. The first model is a ring of polar orbits that move in a plane perpendicular to the binary pericentre direction. We favour this interpretation because it includes the effect of secular perturbations and the disc can survive for Gyr time-scales. The second model is a misaligned ring. Because there is an ambiguity in the orientation of the ring, which could be reflected in the sky plane, this ring either has near-polar orbits similar to the first model or has a 30° misalignment. The misaligned ring, interpreted as the result of a recent collision, is shown to be implausible from constraints on the collisional and dynamical evolution. Because disc+star systems with separations similar to 99 Herculis should form coplanar, possible formation scenarios involve either a close stellar encounter or binary exchange in the presence of circumstellar and/or circumbinary discs. Discovery and characterization of systems like 99 Herculis will help understand processes that result in planetary system misalignment around both single and multiple stars.

Key words: circumstellar matter – stars: individual: 99 Herculis.

1 INTRODUCTION

The *Herschel* key programme DEBRIS (Dust Emission via a Bias-free Reconnaissance in the Infrared/Submillimeter) has observed a large sample of nearby stars to discover and characterize extrasolar analogues to the Solar system's asteroid and Kuiper belts, collectively known as 'debris discs'. The 3.5-m *Herschel* mirror diameter provides 6–7 arcsec resolution at 70–100 μm (Pilbratt et al. 2010), and as a consequence our survey has resolved many discs around stars in the solar neighbourhood for the first time (Matthews et al. 2010; Churcher et al. 2011).[1]

Here we present resolved images of the 99 Herculis circumbinary disc. This system is particularly interesting because unlike most debris disc+binary systems, the binary orbit is well characterized. The combination of a known orbit and resolved disc means we can compare their (different) inclinations and consider circumbinary particle dynamics and formation scenarios.

This system is a first step towards building on the binary debris disc study of Trilling et al. (2007). Their *Spitzer* study found that debris discs are as common in binary systems as in single systems, but tend not to have separations in the 3–30 au range. However, only some of their systems had detections at multiple wavelengths to constrain the disc location and none were resolved, making the true dust location uncertain. Resolved systems such as 99 Her remove this ambiguity and provide crucial information on the disc location, stability and dynamics.

This paper is laid out as follows. We first consider the stellar and orbital properties of the 99 Her system, including the possibility of

⋆Email: gkennedy@ast.cam.ac.uk

[1] *Herschel* is an ESA space observatory with science instruments provided by European-led Principal Investigator consortia and with important participation from NASA.

a third component. Then we consider the *Herschel* image data and several different models that can explain it. Finally, we discuss the implications of these models for the formation of the system.

2 99 HERCULIS

The binary 99 Herculis (HD 165908, HIP 88745, GJ 704AB and ADS 11077) contains the 37th closest F star primary within the volume-limited unbiased nearby stars' sample (Phillips et al. 2010). The Catalogue of Components of Doubles and Multiple systems (CCDM J18071+3034; Dommanget & Nys 2002) lists three components, but using *Hipparcos* proper motions Phillips et al. (2010) find that the 93-arcsec distant C component is not bound to the system. The binary pair has been known since 1859, and consists of an F7V primary orbited by a K4V secondary. The primary is known to be metal poor with [Fe/H] ≈ -0.4 (e.g. Gratton, Carretta & Castelli 1996; Adelman et al. 2000; Takeda 2007) and has an age consistent with the main sequence (6–10 Gyr from isochrone fitting; Nordström et al. 2004; Takeda 2007).

2.1 Binary configuration

To interpret the *Herschel* observations requires an understanding of the binary configuration, which we address first. Typically, the important orbital elements in fitting binary orbits are the semimajor axis, eccentricity and period, which yield physical characteristics of the system (if the distance is known). Regular observations of 99 Her date back to 1859 and the binary has completed nearly three revolutions since being discovered. Additional observations since the previous orbital derivation (Söderhjelm 1999) have allowed us to derive an updated orbit. Aside from a change of 180° in the ascending node (based on spectroscopic data; Abt & Willmarth 2006), the orbital parameters have changed little; the main purpose of re-deriving the orbit is to quantify the uncertainties.

The orbit was derived by fitting position angles (PAs) and separations (ρ) from the Washington Double Star (WDS) Catalog (Mason et al. 2011).[2] We included three additional observations: a *Hubble Space Telescope* Imaging Spectrograph (STIS) acquisition image (epoch 2000.84, PA $= 264^\circ \pm 2^\circ$, $\rho = 0.54 \pm 0.02$ arcsec; Boesgaard et al. 2004), an adaptive optics image taken using the Lick Observatory Shane 3-m telescope with the IRCAL near-infrared (IR) camera as an ongoing search for faint companions of stars in the DEBRIS sample (epoch 2009.41, PA $= 309^\circ \pm 2^\circ$, $\rho = 1.12 \pm 0.02$ arcsec), and a Keck II Second Generation Near TR Camera (NIRC2) L' speckle image taken to look for a third companion (see Section 2.2, epoch 2011.57, PA $= 317^\circ \pm 1^\circ$, $\rho = 1.20 \pm 0.014$ arcsec). For visual data we set uncertainties of 7° to PAs and 0.5 arcsec to separations, for *Hipparcos* data we used 5° and 0.1 arcsec, and for speckle observations without quoted uncertainties we used 2° and 0.04 arcsec. The resulting orbital elements, shown in Table 1, vary only slightly from those derived by Söderhjelm (1999).[3] The best-fitting yields $\chi^2 = 190$ with 399 degrees of freedom. The fit is therefore reasonable, and most likely the χ^2 per degrees of freedom is less than unity because the uncertainties assigned to the visual data are too conservative. If anything, the uncertainties quoted in Table 1 are therefore overestimated. However, visual data can have unknown systematic uncertainties due to individual observers and their equipment so we do not modify them (Hartkopf, Mason & Worley 2001).

Table 1. 99 Her orbital elements, system mass and 1σ uncertainties. The ascending node Ω is measured anticlockwise from north. The longitude of pericentre is measured anticlockwise from the ascending node, and projected on to the sky plane has a position angle of 163° (i.e. is slightly different to 41+116 because the orbit is inclined).

Parameter	Symbol (unit)	Value	Uncertainty
Semimajor axis	a (arcsec)	1.06	0.02
Eccentricity	e	0.766	0.004
Inclination	i (°)	39	2
Ascending node	Ω (°)	41	2
Longitude of pericentre	ω (°)	116	2
Date of pericentre passage	T (yr)	1997.62	0.05
Period	P (yr)	56.3	0.1
Total mass	$M_{\rm tot}$ ($M_\odot$)	1.4	0.1

These data also allow us to derive a total system mass of 1.4 $M_\odot$, where we have used a distance of 15.64 pc (van Leeuwen 2008). While the total mass is well constrained by visual observations, the mass ratio must be derived from either the differential luminosity of each star or radial velocities. We use the spectroscopic mass function derived by Abt & Willmarth (2006), yielding a mass ratio of 0.49, which has an uncertainty of about 10 per cent. The mass ratio from the differential luminosity is 0.58, with a much larger (20 per cent) uncertainty (Söderhjelm 1999). Using the spectroscopic result, the primary (GJ 704A) has a mass of 0.94 $M_\odot$, while the secondary (GJ 704B) is 0.46 $M_\odot$.

The system configuration is shown in Fig. 1 and is inclined such that the primary is currently closer to Earth than the secondary. The position of the B component relative to A on the date it was observed by *Herschel* in late 2010 April was PA $= 314^\circ$ at an observed separation of 1.15 arcsec (22.6 au when deprojected), indicated by grey circles in the figure.

2.2 A third component?

While the STIS images clearly resolve the binary, there is a possible third component with PA $\approx 284^\circ$ and $\rho \approx 0.27$ arcsec that is about 2.4 times as faint as the B component. Scardia et al. (2008) also report a third component (epoch 2005.8) at PA $\approx 50^\circ$ and $\rho \approx 0.228$ arcsec (no magnitude is given). However, while they detected the secondary again in mid-2007, they do not report any detection of the putative tertiary (Scardia et al. 2010). The detected positions are shown as star symbols in sky coordinates in Fig. 2, which shows the motion of the 99 Her system. The system proper motion is $\mu_\alpha \cos\delta = -110.32$ mas yr^{-1}, $\mu_\delta = 110.08$ mas yr^{-1} (van Leeuwen 2008), and accounts for the motion of the primary assuming the orbit derived in Söderhjelm (1999), which is very similar to ours. The small proper-motion uncertainty means STIS and Scardia et al. (2008) cannot have seen the same object if it is fixed on the sky. There is no clear sign of a third component in the residuals from fitting the orbit of the secondary.

To try and resolve this issue we obtained an adaptive optics image of 99 Her at L' (3.8 μm) using the NIRC2 camera at Keck II on 2011 July 27, as shown in Fig. 3. We adopted the narrow camera (10 mas pixel^{-1}) and used a five-point dither pattern with three images obtained at each position consisting of 25 co-adds of 0.181-s integration. The cumulative integration time for the final co-registered and co-added image is 67.875 s. The core of the A component point spread function (PSF) is highly saturated, which

[2] http://ad.usno.navy.mil/wds/

[3] A figure showing the Söderhjelm (1999) orbit is available in the WDS catalogue.

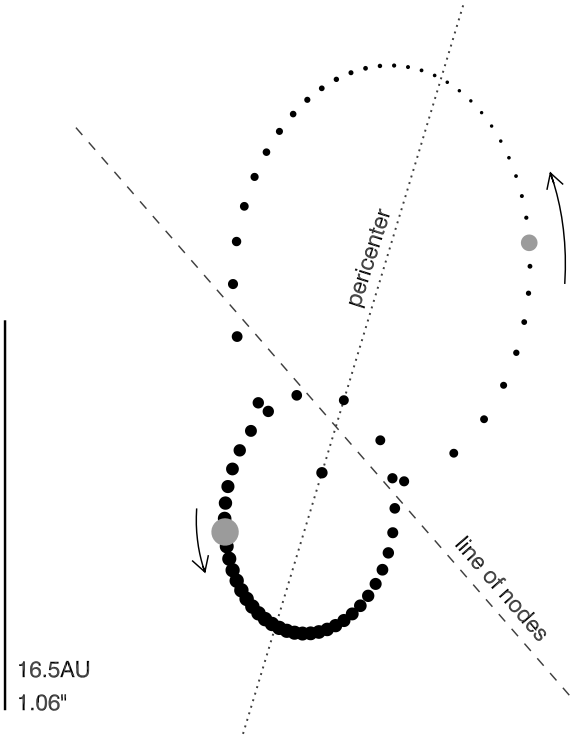

Figure 1. 99 Her binary orbit as seen on the sky, with the line of nodes and pericentre indicated. North is up and east is to the left. The stellar orbits are shown over one (anticlockwise) orbital period with black dots. Grey dots (primary is the larger grey dot) show the positions at the PACS observation epoch. Black dot sizes are scaled in an arbitrary way such that larger dots are closer to Earth. The arrows indicate the direction of motion and the scale bar indicates the binary semimajor axis of 1.06 arcsec (16.5 au).

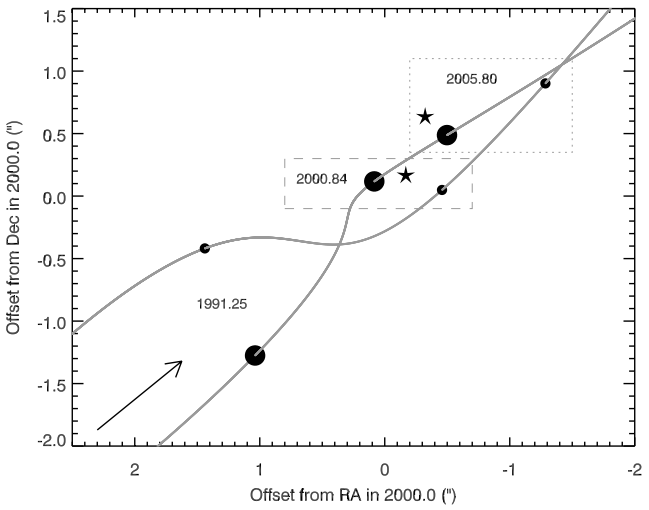

Figure 2. Motion of the 99 Her system (filled dots) in sky coordinates at three epochs. The epochs including the putative third component are enclosed in boxes. The arrow shows the direction of the system centre of mass movement and the distance travelled in 5 years, and the grey lines show the path traced out by each star. Star symbols show the position of the third object observed in the STIS data in 2000 (dashed box) and by Scardia et al. (2008) in 2005 (dotted box).

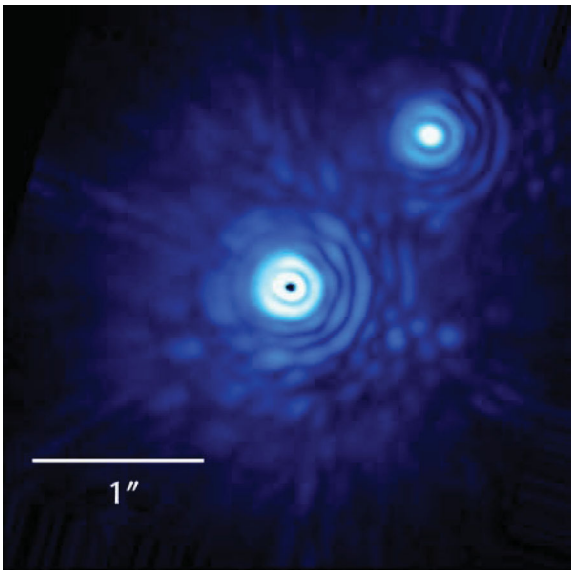

Figure 3. Keck/NIRC2 adaptive optics image of 99 Her at 3.8 μm, cropped to about 1.5 arcsec around the primary. North is up and east is to the left. The saturated A component is at the centre of the frame.

degrades the achievable astrometry. We estimate the position of 99 Her A by determining the geometric centre of the first diffraction ring. The position of 99 Her B is taken from the centroid of the unsaturated core. The PA and separation are quoted above.

There is no detection of the putative 99 Her C within 1.6 arcsec of the primary in the combined image if it is only a factor of 2.4 fainter than the B component, because it would appear 20 times brighter than the brightest speckles. However, if it were closer to the primary than 0.2 arcsec it would currently be too close to detect. If the object was fixed on the sky near either the 2000 or 2005 locations, it would have been detected in the individual pointings of the five-point dither since each NIRC2 pointing has a field of view of 10×10 arcsec^2. To be outside the field of view and still bound to the primary, the tertiary must have an apocentre larger than about 75 au (5 arcsec). An object in such an orbit would have a period of at least 200 years, so could not have been detected near the star in 2005 and be outside the NIRC2 field of view in 2011.

The non-detections by Scardia et al. (2010) and NIRC2 make the existence of the tertiary suspicious. It is implausible that the object was too close to or behind the star both in 2007 and 2011, because at a semimajor axis of 0.23 arcsec (3.5 au) from the primary (similar to the projected separation), the orbital period is 7 years. Therefore, the object would be on opposite sides of the primary, and the two detections already rule out an edge-on orbit. Even assuming a circular orbit, such an object is unlikely to be dynamically stable, given the high eccentricity and small pericentre distance (4.1 au) of the known companion. A tertiary at this separation would be subject to both short-term perturbations and possible close encounters. If the mutual inclination were high enough, it would also be subject to Kozai cycles (Kozai 1962; Lidov 1962) due to the secondary that could result in a high eccentricity and further affect the orbital stability.

While it may be worthy of further detection attempts, the existence of this component appears doubtful and we do not consider it further.

3 IR AND SUB-MM DATA

3.1 Observations

Herschel Photodetector and Array Camera and Spectrometer (PACS; Poglitsch et al. 2010) data at 100 and 160 μm were taken in 2010 April during routine DEBRIS observations. Subsequently, a Spectral and Photometric Imaging Receiver (SPIRE; Griffin et al. 2010) observation was triggered by the large PACS excess, indicating the presence of a debris disc and a likely sub-mm detection. The disc was detected, but not resolved with SPIRE at 250 and 350 μm. A 70-μm PACS image was later obtained to better resolve the disc. Because every PACS observation includes the 160-μm band, we have two images at this wavelength, which are combined to produce a single higher signal-to-noise ratio (S/N) image. All observations were taken in the standard scan-map modes for our survey, mini scan maps for PACS data and small maps for SPIRE. Data were reduced using a near-standard pipeline with the Herschel Interactive Processing Environment (HIPE version 7.0; Ott 2010). We decrease the noise slightly by including some data taken as the telescope is accelerating and decelerating at the start and end of each scan leg.

The high level of redundancy provided by PACS scan maps means that the pixel size used to generate maps can be smaller than the natural scale of 3.2 arcsec pixel^{-1} at 70 and 100 μm and 6.4 arcsec pixel^{-1} at 160 μm via an implementation of the 'drizzle' method (Fruchter & Hook 2002). Our maps are generated at 1 arcsec pixel^{-1} at 70 and 100 μm and 2 arcsec pixel^{-1} at 160 μm. The benefit of better image sampling comes at the cost of correlated noise (Fruchter & Hook 2002), which we discuss below.

In addition to correlated noise, two characteristics of the PACS instrument combine to make interpretation of the data challenging. The PACS beam has significant power at large angular scales; about 10 per cent of the energy lies beyond 1 arcmin and the beam extends to about 17 arcmin (1000 arcsec). While this extent is not a problem in itself, it becomes problematic because PACS data are subject to fairly strong $1/f$ (low frequency) noise and must be high-pass filtered. The result is that a source will have a flux that is 10–20 per cent too low because the 'wings' of the source were filtered out. While this problem can be circumvented with aperture photometry using the appropriate aperture corrections derived from the full beam extent, the uncorrected apertures typically used for extended sources will result in underestimates of the source flux.[4]

Here, we correct the fluxes measured in apertures for 99 Her based on a comparison between PSF-fitted and aperture-corrected measurement of bright point sources in the DEBRIS survey with predictions from their stellar models (based on the calibration of Rieke et al. 2008). These upward corrections are 16 ± 5, 19 ± 5 and 21 ± 5 per cent at 70, 100 and 160 μm, respectively. These factors depend somewhat on the specifics of the data reduction, so are *not* universal. This method assumes that the correction for 99 Her is the same as for a point source, which is reasonable because the scale at which flux is lost due to filtering the large beam is much larger than the source extent. The corrected PACS measurement is consistent with MIPS 70 μm, so we do not investigate this issue further.

The beam extent and filtering is also important for resolved modelling because the stellar photospheric contribution to the image is decreased. Therefore, in generating a synthetic star+disc image to compare with a raw PACS observation, the stellar photospheric flux should be decreased by the appropriate factor noted above. Alternatively, the PACS image could be scaled up by the appropriate factor and the true photospheric flux used.

[4] See http://herschel.esac.esa.int/twiki/bin/view/Public/WebHome for details regarding the PACS beam extent and calibration.

Table 2. *Herschel* photometry of 99 Her. The disc is not detected at 500 μm and can be considered a 3σ upper limit of 24 mJy.

Band	Flux (mJy)	Uncertainty	Method
PACS70	93	10	15-arcsec aperture
PACS100	87	10	15-arcsec aperture
PACS160	80	15	17-arcsec aperture
SPIRE250	44	6	PSF fit
SPIRE350	22	7	PSF fit
SPIRE500	4	8	PSF fit

Table 2 shows the measured star+disc flux density in each *Herschel* image. Uncertainties for PACS are derived empirically by measuring the standard deviation of the same sized apertures placed at random image locations with similar integration time to the centre (i.e. regions with a similar noise level).

The SPIRE observations of 99 Her are unresolved. The disc is detected with reasonable S/N at 250 μm, marginally detected at 350 μm, and not detected at 500 μm. Fluxes are extracted with PSF fitting to minimize the contribution of background objects. Because all three bands are observed simultaneously (i.e. a single pointing), the PSF fitting implementation fits all three bands at once. A detection in at least one band means that all fluxes (or upper limits) are derived at the same sky position.

Additional IR data exist for 99 Her, taken with the Multiband Imaging Photometer for *Spitzer* (MIPS; Rieke et al. 2004). Only the star was detected at 24 μm (270.3 ± 0.1 mJy), but this observation provides confirmation of the 99 Her stellar position in the PACS images relative to a background object 1.8 arcmin away to the south-east (PA $= 120^\circ$) that is visible at 24, 70 and 100 μm. The presence of an excess at 70 μm (98 ± 5 mJy compared to the photospheric value of 30 mJy) was in fact reported by Koerner et al. (2010). They did not note either the circumbinary nature or that the disc may be marginally resolved by MIPS at 70 μm. Because our study focuses on the spatial structure, we use the higher resolution PACS data at 70 μm, but include the MIPS data to model the spectral energy distribution (SED).

3.2 Basic image analysis

Fig. 4 shows the *Herschel* PACS data. Compared to the beam size, the disc is clearly resolved at all three wavelengths. At 160 μm, the peak is offset about 5 arcsec east relative to both the 70- and 100-μm images. However, the disc is still visible at 160 μm as the lower contours match the 70- and 100-μm images well. The 160-μm peak is only 2σ–3σ more significant than these contours. While such variations are possible due to noise, in this case the offset is the same in both 160-μm images, so could be real. The fact that the peak extends over several pixels is not evidence that it is real, because the pixels in these maps are correlated (see below). If real, this component of the disc or background object cannot be very bright at SPIRE wavelengths because the measured fluxes appear consistent with a blackbody fit to the disc (see Section 4). Based on an analysis of all DEBRIS maps (that have a constant depth), the chance of a 3σ or brighter background source appearing within 10 arcsec of 99 Her at 160 μm is about 5 per cent (Thureau et al., in preparation). Given that the 160-μm offset is only a 2σ–3σ

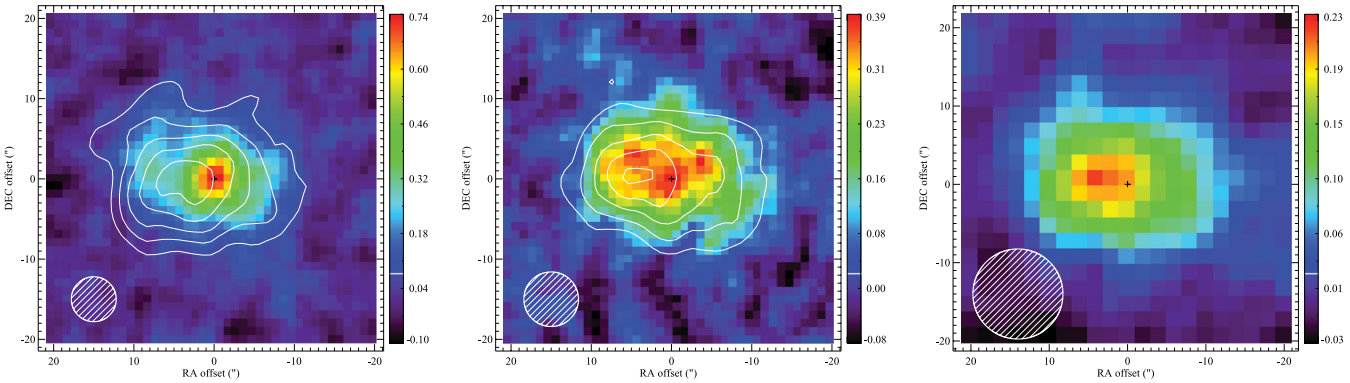

Figure 4. *Herschel* PACS images of the 99 Her system at 70 μm (left) 100 μm (centre) and combined 160 μm (right). North is up and east is to the left. Colour bars show levels in units of mJy arcsec^{-2}. Contours in the left two panels show the 160-μm data from each observation in five levels from 3σ to 9σ. The images are centred on the primary position (plus symbol) derived from the 70-μm image. Hatched circles show the FWHM beam sizes of 5.6, 6.8 and 11.5 arcsec at 70, 100 and 160 μm, respectively.

effect (i.e. could be a 2σ–3σ background source superimposed on a smooth disc), the probability is actually higher because the number of background sources increases strongly with depth. These objects have typical temperatures of 20–40 K (e.g. Amblard et al. 2010), so could easily appear in only the 160-μm image, particularly if the disc flux is decreasing at this wavelength.

We now analyse the PACS images using two-dimensional (2D) Gaussian models to estimate the disc size, inclination and position angle. A 2D Gaussian fits the star-subtracted PACS 100-μm image fairly well, with major and minor full-width at half maxima (FWHMs) of 17.7 and 12.8 arcsec at a position angle of 78°. Quadratically deconvolving from the 6.7-arcsec FWHM beam assuming a circular ring implies an inclination of 48° from face-on and an estimated diameter of 250 au. Gaussian fitting to star-subtracted images at both 70 and 160 μm yields similar results.

As noted above, estimation of uncertainties in these parameters is non-trivial due to correlated noise, but made easier by the constant depth of our survey. By inserting the best-fitting Gaussian to the star-subtracted image of the 99 Her disc from the 100-μm image into 438 other 100-μm maps at high coverage positions offset from the intended target, we obtain a range of fit parameters for hundreds of different realizations of the same noise. This process yields an inclination of $45^\circ \pm 5^\circ$ and PA of $75^\circ \pm 8^\circ$. Repeating the process, but using the best-fitting Gaussian for the 70-μm image yields an inclination of $44^\circ \pm 6^\circ$ and PA of $68^\circ \pm 9^\circ$. Though the inclination of the disc is similar to the binary, the position angle is significantly different from the binary line of nodes of $41^\circ \pm 2^\circ$. This difference means that the disc and binary orbital planes are misaligned.

As a check on the above approach, we can correct for the correlated noise directly. Fruchter & Hook (2002) show that for a map that has sufficiently many dithers (corresponding in our case to many timeline samples across each pixel), a noise 'correction' factor of $r/(1-1/3r)$ can be derived, where r is the ratio of natural to actual pixel scales and is 3.2 for our PACS maps. A correction factor of 3.6 for the measured pixel-to-pixel noise is therefore required when estimating the uncertainty on a fitted Gaussian. Including this factor at 70 μm and calculating the uncertainty by the standard $\Delta\chi^2$ method yields an inclination of $42^\circ \pm 7^\circ$ and a PA of $68^\circ \pm 9^\circ$. At 100 μm, the result is an inclination of $44^\circ \pm 6^\circ$ and a PA of $76^\circ \pm 8^\circ$. These results are therefore almost exactly the same as the empirical method used above and therefore lead to the same conclusion of misalignment.

As will become apparent in Section 5, there is reason to believe that the disc plane could be perpendicular to the binary pericentre direction. The projection of the binary pericentre direction on the sky plane has a PA of $163^\circ \pm 2^\circ$, and a line perpendicular to this has a PA of $73^\circ \pm 2^\circ$. Therefore, the observed disc position angle of about 72° is consistent with being at 90° to the binary pericentre direction.

4 SED

The combination of all photometry for 99 Her allows modelling of the SED. The model is separated into two components: a stellar atmosphere and a disc. Due to being fairly bright ($V \sim 5$ mag), the system is saturated in the Two Micron All-Sky Survey (2MASS) catalogue. However, sufficient optical photometry for each individual star and the pair exists (Henry & McCarthy 1993; Hauck & Mermilliod 1997; Perryman & ESA 1997; Mermilliod 2006), as well as IR measurements of the AB pair from *Akari* and *IRAS* (Moshir & et al. 1990; Ishihara et al. 2010). These data were used to find the best-fitting stellar models via χ^2 minimization. This method uses synthetic photometry over known bandpasses and has been validated against high-S/N MIPS 24-μm data for DEBRIS targets, showing that the photospheric fluxes are accurate to a few per cent for AFG-type stars. The stellar luminosities ($L_{\star,\mathrm{A}} = 1.96\,\mathrm{L}_\odot$, $L_{\star,\mathrm{B}} = 0.14\,\mathrm{L}_\odot$) and IR fluxes of the individual components are consistent with the fit for the pair ($L_{\star,\mathrm{AB}} = 2.08\,\mathrm{L}_\odot$). The fit for the AB pair is shown in Fig. 5.

The spatial structure of the disc can be modelled with dust at a single radial distance of 120 au (i.e. thin compared to *Herschel's* resolution, Section 5), so disc SED modelling can be decoupled from the resolved modelling once this radial distance is known. Because we have measurements of the disc emission at only five wavelengths, we cannot strongly constrain the grain properties and size distribution. We fit the data with a blackbody model and then compare the data with several 'realistic' grain models (Li & Greenberg 1997; Augereau et al. 2001; Wyatt & Dent 2002).

In fitting a blackbody we account for inefficient grain emission at long wavelengths by including parameters λ_0 and β, where the blackbody is modified by a factor $(\lambda_0/\lambda)^\beta$ for wavelengths longer than λ_0. The best-fitting model has a temperature of 49 K and fractional luminosity of $L_{\mathrm{disc}}/L_\star = 1.4 \times 10^{-5}$. The SPIRE data are near the confusion limit of about 6 mJy, so the parameters

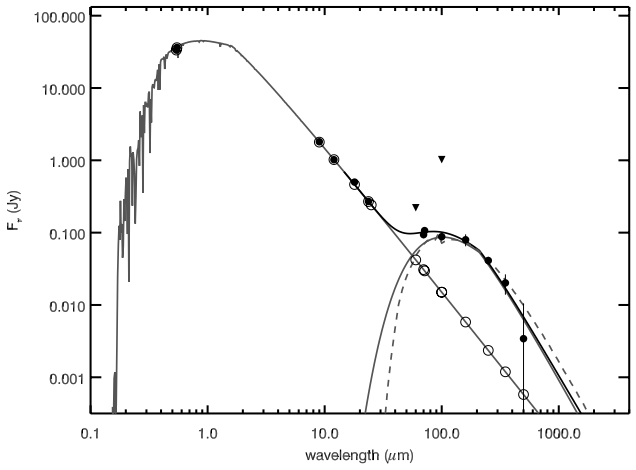

Figure 5. SED for the 99 Her system (both stars) showing the stellar and disc models (grey lines) and the star+disc model (black line). The blackbody disc model is the solid grey line and the physical grain model is the dashed line. Photometric measurements are shown as black filled circles and synthetic photometry of the stellar atmosphere is shown as open circles ($U - B$, $B - V$ and $b - y$ colours, and $m1$ and $c1$ Stromgren indices were fitted but are not shown here). Black triangles mark upper limits from *IRAS* at 60 and 100 μm.

β and λ_0 are unconstrained within reasonable limits by the data (based on previous sub-mm detections for other discs we fix them to $\lambda_0 = 210$ μm and $\beta = 1$ in Fig. 5; Wyatt et al. 2007b).

Assuming that grains absorb and emit like blackbodies, the radial dust distance implied by 49 K is 45 au. Because the disc is observed at a radius of 120 au (i.e. is warmer than expected for blackbodies at 120 au), the dust emission has at least some contribution from grains small enough to emit inefficiently in the 70–350 μm wavelength range. Because the SED alone is consistent with a pure blackbody (i.e. with $\beta = 0$), we cannot make such a statement without the resolved images. However, actually constraining the grain sizes is difficult because temperature and emission are also affected by composition. We fit the data by generating disc SEDs for grains at a range of semimajor axes and choosing the one with the lowest χ^2. If the dust semimajor axis is different from the observed semimajor axis of 120 au, the model parameters are changed and the model recalculated, thus iterating towards the best fit.

We model the dust with a standard diameter (D) distribution $n(D) \propto D^{2-3q}$, where $q = 1.9$ [equivalently, $n(M) \propto M^{-q}$ where M is mass; O'Brien & Greenberg 2003], with the minimum size set by the blowout limit for the specific composition used (about 1.4 μm) and a maximum size of 10 cm. The size distribution probably extends beyond 10 cm, but objects larger than 10 cm contribute negligibly to the emission because the size distribution slope means that smaller grains dominate. Preliminary tests found that icy grains provided a much better fit than silicates. To refine the grain model so that the SED and resolved radius agree, we introduced small amounts of amorphous silicates to the initially icy model. The grains are therefore essentially ice mixed with a small fraction ($f_{\rm sil} = 1.5$ per cent) of silicate. The icy grain model is shown as a dotted line in Fig. 5. This model has a total dust surface area of 14 au^2 and a mass of the order of 10 $M_\oplus$ if the size distribution is extrapolated up to 1000-km-size objects.

The parameters of this model are degenerate for the data in hand; for example the size distribution could be shallower and the fraction of silicates higher (e.g. $q = 1.83$ and $f_{\rm sil} = 4$ per cent). If we allow the minimum grain size to be larger than the blowout limit, the disc is well fitted by amorphous silicate grains with $q = 1.9$ and $D_{\rm bl} = 10$ μm. The disc spectrum can even be fitted with a single size population of 25-μm icy grains. However, the predictions for the flux at millimetre wavelengths depend on the size distribution, with lower fluxes for steeper size distributions. Therefore, grain properties and size distribution can be further constrained in the future with deep (sub)mm continuum measurements.

In summary, it is hard to constrain the grain sizes or properties. There is a difference in the required minimum grain size that depends on composition. Because icy grains are reflective at optical wavelengths, a detection of the disc in scattered light could constrain the albedo of particles, and therefore their composition.

5 SPATIAL STRUCTURE

The PACS images of the 99 Her disc are resolved, which allows modelling of the spatial distribution of grains that contribute to the observed emission at each wavelength. We compare synthetic images with the *Herschel* observations in several steps: (i) Generate a 3D distribution of the surface area $\sigma(r, \theta, \phi)$, where the coordinates are centred on the primary star. (ii) Generate a radial distribution of grain emission properties. Because the SED can be modelled with blackbody grains at 49 K and the spatial structure modelled with a narrow ring, there is no real need for a radial temperature dependence and the grain properties are only a function of wavelength: $P(\lambda) = B_\nu(49\,{\rm K}, \lambda)$. Practically, we use a radial temperature dependence $T \propto r^{-1/2}$ centred on the primary, normalized so that the disc ring temperature is 49 K. This approach ensures that temperature differences due to non-axisymmetries (negligible for 99 Her) are automatically taken into account. (iii) Generate a high-resolution model as viewed from a specific direction. The emission in a single pixel of angular size x from a single volume element in the 3D model dV viewed along a vector $\mathcal{R}$ is $dF_\nu(\lambda, r, \theta, \phi) = P(\lambda)\sigma(r, \theta, \phi){\rm d}V$, where ${\rm d}V = x^2 d^2 {\rm d}\mathcal{R}$, so d$\mathcal{R}$ is the length of the volume element, and d is the distance to the particles from Earth (Wyatt et al. 1999). The emission is derived by integrating along the line of sight $\mathcal{R}$ for each pixel in the synthetic image. The photospheric fluxes for each star (decreased by the factors noted in Section 3.1) are placed in the relevant pixels in this step. (iv) Convolve the high-resolution model with a high-resolution telescope+instrument beam, for which we use interpolated and rotated PACS images of the star Arcturus.[5] (v) Degrade the resolution to match the data. (vi) Generate a map of residuals, defined by (observed − model)/uncertainty, where the uncertainty is the pixel-to-pixel rms for that observation. We compute the model χ^2 from pixels in a square crop around the disc.

A minor consideration is that in the general circumbinary case, the disc temperature is not axisymmetric because the disc orbits the centre of mass, not the primary. An axisymmetric disc is therefore subject to a temperature asymmetry such that it will be slightly hotter, and therefore brighter, where the distance to the primary is smallest. This 'binary offset' asymmetry will rotate with the primary and will be most pronounced in the coplanar case. The result of this effect is similar to the offset caused by perturbations from an eccentric object ('pericentre glow'; Wyatt et al. 1999). However, the pericentre glow is offset towards the pericentre of the perturbing

[5] The observations are reduced in sky coordinates, so the spacecraft orientation is different for each observation and the PSF must be rotated accordingly. This rotation step could be avoided by reducing both in spacecraft coordinates.

object, so does not rotate unless the perturbing object's pericentre precesses. The offset from the primary and the pericentre glow are completely independent effects. Therefore, if the pericentre glow effect is present, it will reinforce and cancel the binary offset effect, depending on the relative magnitude of each offset. The magnitude of the binary offset effect is negligibly small ($\lesssim$1 per cent) because the disc radius is much larger than the binary separation. Because our model is centred on the system centre of mass, this effect is taken into account anyway. We discuss the effect of the binary on pericentre glow in Section 5.1.1.

To fit the data requires a handful of parameters, some are required for all models and some are model specific. The disc surface area, temperature, radius, width and total opening angle are the five physical parameters for a ring. The sky position angle and inclination are two further parameters that set the orientation, but can be fixed if the disc plane is assumed to be aligned with the binary. In addition, each observation has the stellar RA and Dec. as parameters to allow for the 2-arcsec 1σ pointing accuracy of *Herschel*. The position at 160 μm is tied to the 100-μm position. There are therefore 11 possible parameters to fit for the resolved observations at 70, 100 and 160 μm. We fix the disc temperature at 49 K in all cases.

From the basic analysis (Section 3.2), a simple ring coplanar with the binary does not appear a viable option. To emphasize this point, we show 70- and 100-μm images of the best-fitting coplanar model in Fig. 6. This model was generated by the steps outlined above, and the rightmost three panels are the results of steps iv (convolved model), iii (high-resolution model) and vi (residuals). We fix the disc width to 20 au, the opening angle to 5°, and the position angle and inclination to the binary plane, so there are six free parameters (surface area, radius and two pairs of RA/Dec. sky positions). While we include the 160-μm image in the fitting, it does not constrain the fit strongly due to low S/N and always shows $\sim$2σ residual structure due to the offset peak. For comparison with the models below, the χ^2 value for all three PACS bands is 4278 with 3797 degrees of freedom. The positive and negative residuals (rightmost panels) show that the disc ansae in the model have the wrong orientation at both wavelengths. It is clear that any structure symmetric about the binary line of nodes will not be consistent with the observations because the position angle is significantly different.

An alternative explanation for the misalignment between the observed position angle and the binary line of nodes could be that the dust does in fact lie in the binary plane, but that the particles are on eccentric orbits with common pericentre directions (i.e. the disc is elliptical and offset from the binary). In principle, the observations can constrain the eccentricity and pericentre direction. However, this model fails because the eccentricity needed to match the observed position angle is too extreme. In order to obtain an ellipse that lies in the binary orbital plane and has a position angle and aspect ratio similar to the observations requires eccentricities of $\gtrsim$0.4. The eccentricity of these particles is so high that (i) the ring is significantly offset from the star and (ii) the ring has an extreme pericentre glow asymmetry at all wavelengths caused by particles residing at different stellocentric distances. Because the PACS 70-μm image shows that the star lies very near the disc centre, such a strong offset is ruled out.

We now consider two relatively simple models that account for the misalignment between the disc and binary orbital planes. The first is based on the expected secular evolution of circumbinary particles, and the second is a simple misaligned ring where the disc position angle and inclination are free parameters.

5.1 Secularly perturbed polar ring

In this section, we consider a ring inspired by the secular evolution of circumbinary particles. This approach ensures that the disc is stable over the stellar lifetime and encompasses the particle dynamics dictated by the binary. We first outline the dynamics of circumbinary particles and then show the model for the 99 Her disc.

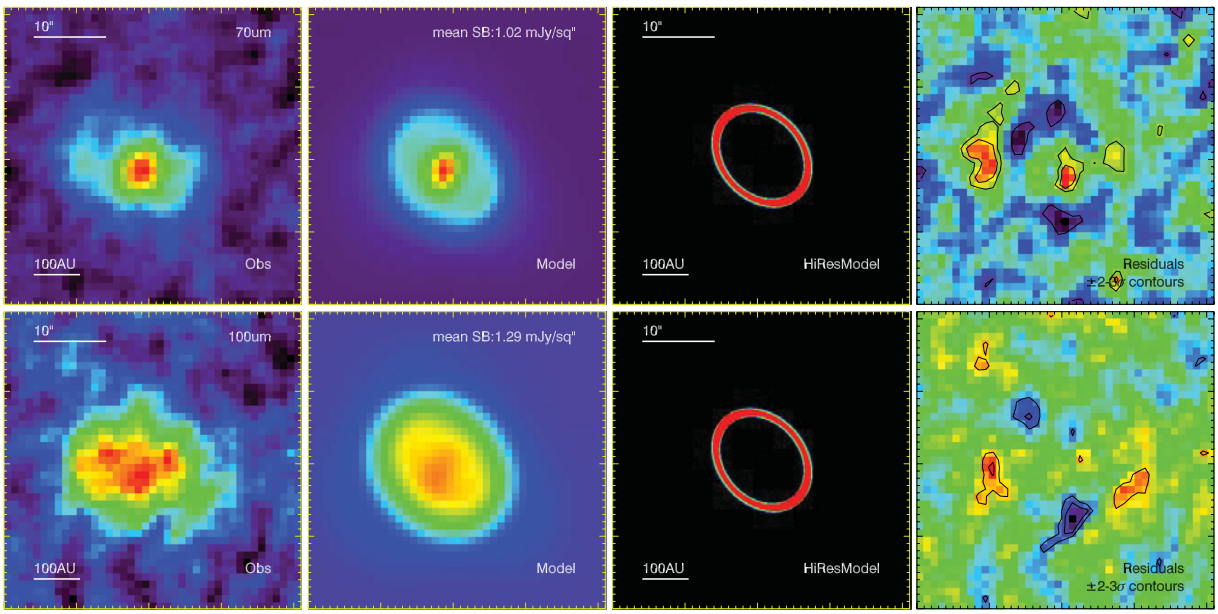

Figure 6. Simple ring model where the disc is aligned with the binary orbital plane, compared to the PACS 70 (top row) and 100 μm (bottom row) observations. North is up and east is to the left. Columns show the data, model convolved with the PACS beam, a high-resolution model and the data–model residuals from left to right. The model includes stellar photospheric fluxes, which lie in two pixels near the ring centre but are not visible in the high-resolution plot. In the residual plots, contours show ±2 and 3σ in units of pixel-to-pixel rms.

5.1.1 Dynamics

Particle dynamics are important for evolution and stability in the 99 Her system. A circumbinary disc will have its inner edge truncated, while circumstellar discs around either component can be truncated at their outer edges. In addition, secular perturbations lead to precession of test particles' nodes coupled with inclination variations. We explore these dynamics using the *Swift* Hierarchical Jacobi Symplectic (HJS) integrator (Beust 2003).

In general, disc truncation allows us to place limits on possible locations for disc particles. However, in the case of 99 Her, there is no evidence for disc components orbiting only one star, and the apparent circumbinary disc extent lies well beyond ∼30–60 au stability limit at any inclination (Wiegert & Holman 1997; Doolin & Blundell 2011).

Circumbinary particles also undergo long-term dynamical evolution due to secular perturbations. Because the binary has a small mass ratio and high eccentricity, the dynamics are not well described by the circular restricted three-body problem, commonly applied in the case of debris discs perturbed by planets. Similar dynamics have previously been explored in the context of the HD 98800 system (Verrier & Evans 2008, 2009) and more generally (Farago & Laskar 2010; Doolin & Blundell 2011).

These studies show that the inclination (i) and line of nodes (Ω) of circumbinary particles evolve due to perturbations from the binary. Depending on the binary eccentricity and particle inclination, Ω can circulate (increase or decrease continuously) or librate (oscillate about 90° or 270°). Particles with low inclinations stay on low-inclination orbits, thus sweeping out a roughly disc- or torus-like volume over long time-scales. Higher inclination particles are subject to nodal libration and large inclination variations, thus sweeping out large parts of a sphere around the binary. Most importantly for 99 Her, the orbits of particles with $\Omega \approx 90°$ (or 270°) and on near polar orbits will not change much due to secular evolution, thus sweeping out a polar ring.

Fig. 7 shows the secular evolution of 23 particles on initially circular orbits in complex inclination space. All particles have initial nodes of 90° relative to the binary pericentre and inclinations spread evenly between 0° and 180° and are integrated for 1 Gyr (i.e. there are no other significant effects on such long time-scales). At 120 au, the time taken for a particle to complete one cycle of secular evolution (make a loop in Fig. 7) varies in the range of $2–7 \times 10^5$ yr, with larger loops taking longer. These times will also scale with particle semimajor axis. Particles 1–12 are those with initial inclinations between 0°–90° that are sufficient to describe the range of spatial structures as we cannot distinguish between prograde and retrograde orbits.

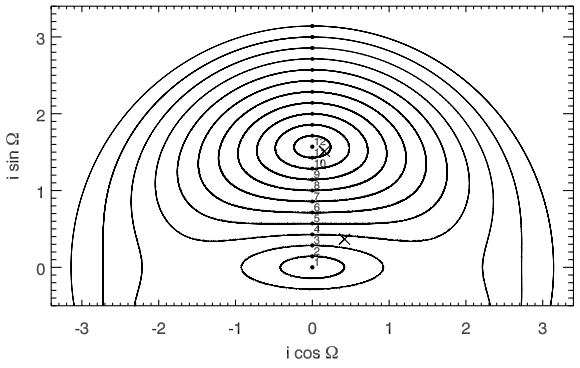

Figure 7. Secular evolution of circumbinary particles in inclination (i) and line of nodes (Ω) space. Particles begin at dots and move along the curves due to perturbations from the binary. Particles that would appear reflected in the x-axis duplicate the spatial distribution, so are not shown. Crosses show the current location of particles in the two interpretations of the transient ring model (Section 5.2). Over time these particles will sweep out curves similar to particles 4 and 11. The long-term structure of the transient ring will therefore appear similar to either panel 4 or 11 in Fig. 8, depending on which inclination is correct.

The particles can be split into two groups: those with low inclinations whose nodes circulate (1–3) and those with high inclinations whose nodes librate about 90° (4–12). The dividing line (separatrix) between these families for the binary eccentricity of 0.76 is 21° when $\Omega = 90°$ (or 270°; Farago & Laskar 2010). While particles in the first group have $i < 21°$ when $\Omega = 90°$, their inclinations when $\Omega = 0°$ (or 180°) can be as high as 90°. Thus, particles near the separatrix will sweep out an entire spherical shell during their secular evolution. Similarly, particles near the separatrix but in the second group also sweep out a spherical shell, though the orbital evolution is different.

To visualize the structures swept out by these families of particles due to secular perturbations, Fig. 8 shows the resulting debris structures for particles that follow each of the trajectories 1–12 from Fig. 7 (left to right and down). The structures are oriented as they would be seen on the sky in the 99 Her system (i.e. have the same orientation with respect to the binary orbit shown in Fig. 1). Each structure was generated by taking the relevant particle at each time step and spawning 1000 additional particles spread randomly around the orbit. This process was repeated for every time step, thus building up the spatial density of a family of particles that follow a specific curve in Fig. 7. These structures are optically thin, which makes interpreting them somewhat difficult. We have included a scaled version of the binary orbit from Fig. 1 in some panels in an attempt to make the orientations clearer.

The first (top left) panel shows a circular orbit coplanar with the binary. The position angle is the binary line of nodes, and Fig. 6 shows why a disc in the plane of the binary is not a satisfactory match to the observations. The second and third panels are still symmetric about the binary orbital plane, but have a wider range of inclinations and are an even poorer match to the observations. Panel 3 shows that while particle inclinations are restricted for $\Omega = 90°, 270°$, they can be large for $\Omega = 0°, 180°$ and result in a 'butterfly' structure when viewed down the binary pericentre direction.

The remaining panels are for particles 4–12, whose nodes librate and for which the plane of symmetry is perpendicular to the binary pericentre direction. In panel 4 the range of nodes and inclinations is so large that a particle sweeps out nearly an entire spherical shell during a cycle of secular evolution (i.e. the particle is near the separatrix). This range decreases as the initial inclination nears a polar orbit, at which point the orbital elements do not evolve and the resulting structure appears in panel 12 as a simple ring. The key difference from the ring in panel 1 is that this ring's position angle is perpendicular to the sky projection of the binary pericentre direction and, as noted in Section 3.2, is therefore similar to the observed PA in the PACS images.

Secular perturbations from the binary also affect the long-term evolution of particle eccentricities and pericentre longitudes. These effects are taken into account by our n-body approach. However, we noticed that the eccentricities imposed ('forced') on the particles are lower than would be expected for a lower mass companion. Further n-body simulations of coplanar particles show that for 99 Her with a mass ratio of 0.49, the forced eccentricity at 120 au is about 0.03, but if the mass ratio were 0.05 the forced eccentricity is 0.1.

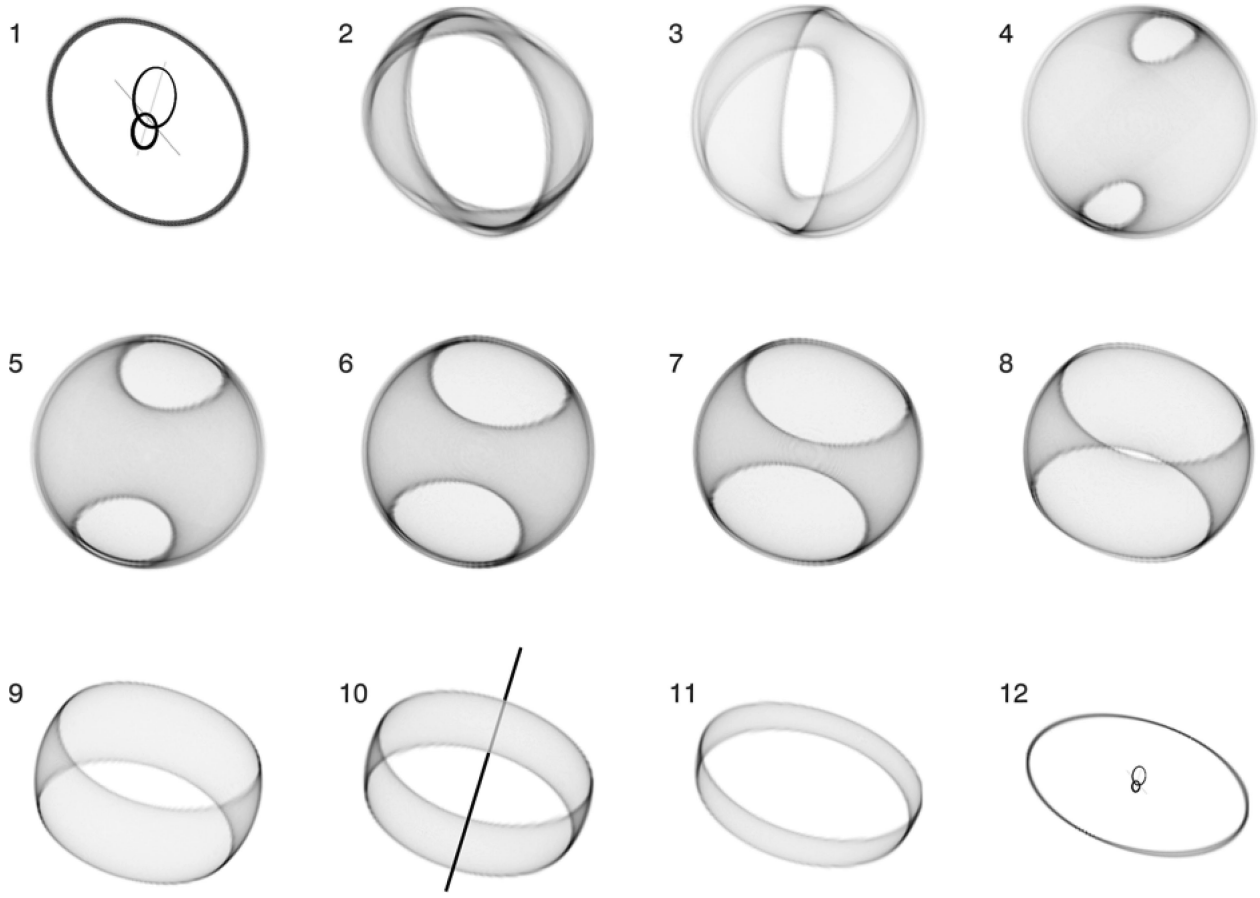

Figure 8. Debris structures derived from the secular evolution of particles 1–12 in Fig. 7 as they would be seen in the 99 Her system. In panels 1 and 12, we have included the binary orbit from Fig. 1. The orbit is not to scale in panel 1 for better visualization, but is in panel 12. Panel 10 includes a line along the binary pericentre direction that is obscured by the ring to show the orientation. In panels 1–3, particles' nodes circulate and the binary orbital plane is the plane of symmetry. In panel 1, the coplanar case, the position angle of the disc is aligned with the line of nodes. In panel 3, the binary is nearly surrounded by a broad shell of particles. In panels 4–12, particles' nodes librate and the plane of symmetry is perpendicular to the binary pericentre direction. In panels 7–12, the observed position angle is perpendicular to the binary pericentre.

This lack of significant eccentricity forcing is visible by its absence in Fig. 8, where the structures would be much broader if there were a large range of particle eccentricities. For example, if the mass of the secondary in the 99 Her system were significantly smaller, the model in panel 1 would become broader and offset from the binary centre of mass, resulting in a small pericentre glow effect.

This dependence suggests that a circumbinary disc's structure may help constrain the binary mass ratio in cases where it is uncertain. However, we cannot apply this idea to make a better estimate of the 99 Her mass ratio because the PACS observations do not have enough resolution. In addition, at high inclinations the particle behaviour is more complicated, because polar particles switch between prograde and retrograde orbits and do not follow simple circles in complex eccentricity space.

5.1.2 Polar ring model

We now use the models from Fig. 8 to fit the PACS observations. The model has only seven free parameters: the particle semimajor axis and initial inclination, the surface area of dust and the same four RA/Dec. positions. The dust temperature is fixed to 49 K. Using a semimajor axis of 120 au, each panel was compared to the PACS images, setting the surface area in grains for each model to obtain the least residual structure. Of these we found that panel 9 was the best fit, as shown in Fig. 9. These particles follow near-polar orbits, so we call this model a 'polar ring'. We find $\chi^2 = 3202$. In terms of χ^2, the results for panels 8 and 10 are similar, but slightly higher. The uncertainty in the initial inclination is therefore about 10°, and for the semimajor axis about 10 au. This model is much better than the coplanar model of Fig. 6, with no overlapping residual structure at 70 and 100 μm. The particles likely occupy a wider range of orbits than a single semimajor axis with some non-zero eccentricity, which may account from some minor (2σ) structure in the residuals at the disc ansae at 70 μm. However, given that this model stems directly from the secular evolution, has very few free parameters and accounts for the structure in all PACS images, we consider it a plausible explanation.

5.2 Transient ring model

A simple circular ring is a natural model to fit to the observations. This model has eight free parameters, with the width of the ring fixed at 20 au and the opening angle fixed to 5°. As expected from the simple analysis in Section 3.2, the position angle of this ring is not aligned with the binary line of nodes, and is therefore misaligned with the binary orbit.

The interpretation depends on the orientation of the best fit. A misaligned ring with polar orbits and the correct line of nodes

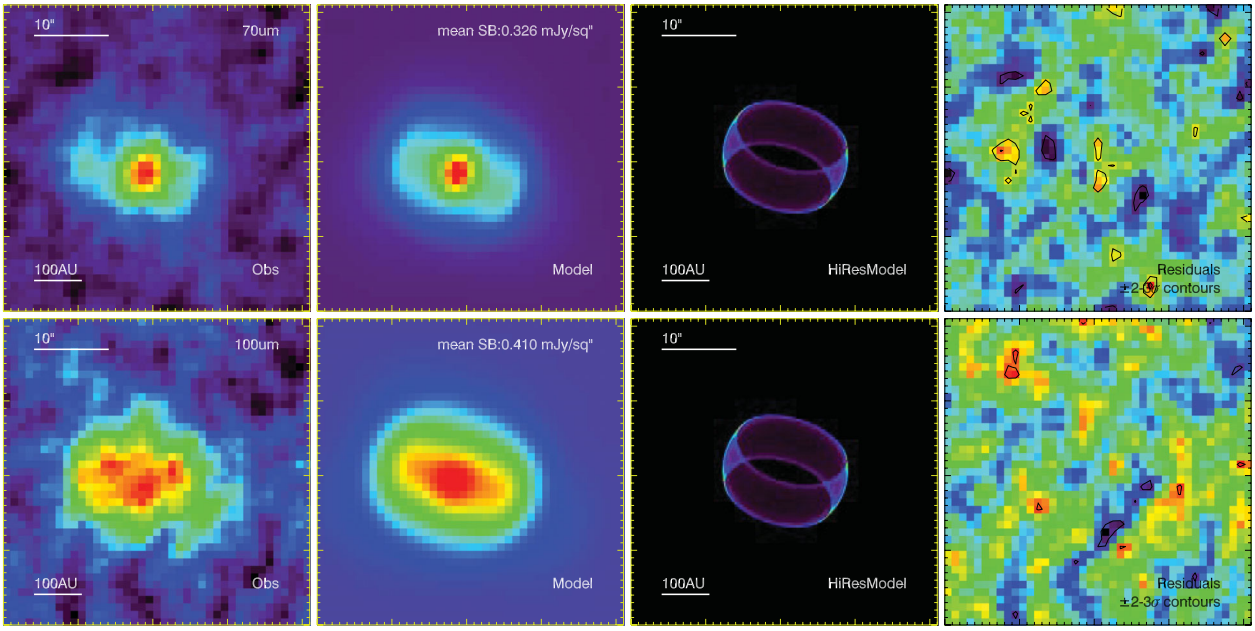

Figure 9. Polar ring model compared to the PACS 70 (top row) and 100 μm (bottom row) observations. Layout is the same as for Fig. 6.

would be considered further evidence in favour of the above polar ring model. A ring with a non-polar orientation will be spread into a broad structure like one of the panels in Fig. 8 by secular perturbations. The ring cannot be long-lived and could therefore be the aftermath of a recent collision, seen after the collision products have sheared into a ring, but before secular perturbations destroy the ring structure. Thus, we call this model a 'transient ring'.

This model is shown in Fig. 10 and is a reasonable match to the PACS observations. However, the residuals at 70 μm show that the ring produces a structure that is slightly too elliptical, compared to the more rectangular structure that is observed and reproduced by the polar ring. This model also has less emission at the stellar position than is observed. For this model, $\chi^2 = 3304$. The disc is inclined 53° from face-on and the PA is 81°. The uncertainties are similar to those derived for the Gaussian fits in Section 3.2. The minimum relative inclination between the disc and binary orbital planes is therefore 32°, with a line of nodes with respect to the binary orbit of 139°.

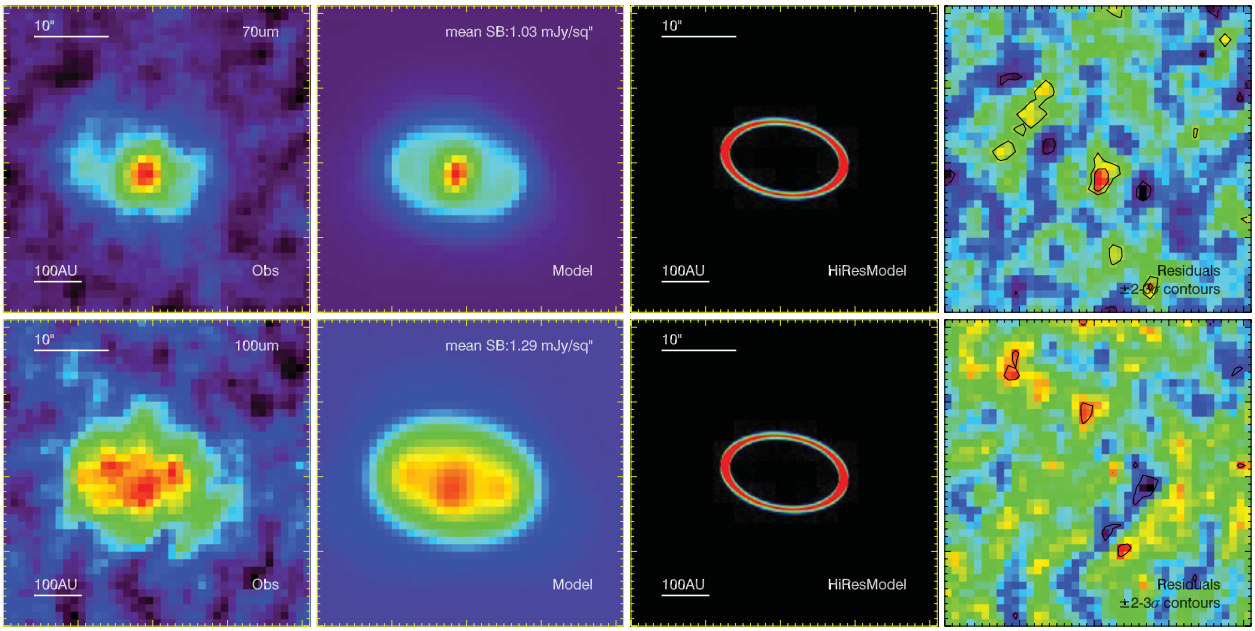

Figure 10. Transient ring model compared to the PACS 70 (top row) and 100 μm (bottom row) observations. Layout is the same as for Fig. 6.

However, the inclination between the disc and the binary plane could also be 87° if the disc were mirrored in the sky plane, which means that the particles have near-polar orbits. These orbits are nearly the same as in panel 12 of Fig. 8 (the narrow polar ring) because the line of nodes with respect to the binary orbit is 276°.

These two interpretations correspond to two points in Fig. 7, shown as crosses. Over time the particles would spread around to make two more lines similar to those drawn. The particles in the lower inclination case are close to the separatrix, and would therefore sweep out a near-spherical shell like panel 4 of Fig. 8. In this case, the long-term evolution produces structures that have the wrong position angle and are a poor match to the observations. The higher inclination case is very nearly a polar ring and would look very similar to panel 11. Such a result is expected because we found above that the polar ring model works well, and argues in favour of the polar ring interpretation.

We can in fact improve this simple ring model by increasing the total disc opening angle (i.e. allowing a larger range of inclinations), which emulates the range of inclinations that result from the secular evolution. We find a best fit when the particle inclinations are 25° (total opening angle of 50°), where $\chi^2 = 3210$. This model looks very similar to the preferred polar ring model above, but is not generated in the same way, and will therefore change somewhat due to secular perturbations over time because the disc is not perfectly polar.

6 DISCUSSION

We strongly favour the polar ring model as the best explanation of the disc structure surrounding 99 Her. The polar ring is stable for the stellar lifetime and takes the secular dynamics into account. The transient ring model, where the disc orientation is not fixed, also finds that the disc particles can have polar orbits. However, because the ring could be mirrored in the sky plane and appear the same, the ring could be misaligned with the binary orbital plane by about 30°. Based on χ^2 and the residuals, the polar ring is marginally preferable over the transient ring. However, given that a more realistic model with a range of particle radii and inclinations could improve the fit in each case, we do not assign much importance to the relatively small χ^2 differences. Instead, we consider several constraints on the collisional evolution that argue against the transient ring interpretation.

By considering the time-scales for collisions and secular evolution, we can estimate the likelihood of observing the products of a collision as a transient ring before it is spread into a broader structure. Based on the observed radius and total cross-sectional area, the collisional lifetime of grains just above the blowout size is about a million years (Wyatt et al. 2007a). The emission could last much longer if larger objects exist in the size distribution, and the lifetime scales with the maximum size as $\sqrt{D_{\rm max}/D_{\rm bl}}$, so depends on the size of the largest fragment created in the collision. If the largest fragments are at least 1 mm in size, the lifetime is at least 50 Myr, and we would expect the collisional cascade to be detectable for this length of time. The secular precession time-scale is about 0.5 Myr, and it is reasonable to assume that the ring structure would be erased by secular perturbations within 10 secular time-scales. Thus, the collisional products would be observable as a ring for only 5 Myr. Because the collision time is longer than the secular time, the collision products would spend at most a tenth of their lifetime appearing as a misaligned ring, and the remainder as a broader structure. That is, assuming such a collision did occur, we have less than a 1:10 chance of observing the collision products as a ring that looks like the *Herschel* observations.[6]

While 1:10 is not unreasonable, this estimate does not consider the object that must be destroyed to generate the observed dust or the plausibility of a 1-mm maximum size. To produce the observed fractional luminosity, a parent body of at least 600 km in diameter must be broken into blowout-sized grains. With the more realistic assumption that the collision produced a range of grain sizes, the parent body must be larger, about 2000 km if grains were as large as the 1 mm assumed above (assuming $q = 11/6$). Under the more realistic assumption of a wide range of fragment sizes, up to 1 km say, the parent body would need to be roughly Earth sized. However, for such large fragments the dust lifetime would be 50 Gyr and the chance of observing the structure as a ring very unlikely (1:10 000).

We can estimate the ability of collisions to smash large objects into small pieces by considering their strength and possible collision velocities. The specific energy needed for catastrophic disruption, where the largest collision product is half the original mass (i.e. very large), is roughly 10^{11} erg g^{-1} for objects 2000 km in size (Stewart & Leinhardt 2009). The energy needed to disrupt an object so that the collision products are all very small must be larger. The maximum collision energy possible for circular orbits is for a collision between two equal-sized objects on prograde and retrograde orbits. The collision energy assuming such an impact at twice the orbital velocity of a few km s^{-1} at 100 au is a few 10^{10} erg g^{-1}. Therefore, only in the most optimistic (highest velocity) case is the collision energy sufficient to catastrophically disrupt 2000-km objects. In the event of a disruption, the lifetime of the collision products will be very long because the largest remnant is about 1000 km in size. In the more realistic case where collision velocities are set by object eccentricities and inclinations, disruption of large objects at large semimajor axes is even more difficult. This difficulty, combined with the smaller amount of starlight intercepted at such distances, means that single collisions only produce a minor increase over the background level of dust (Kenyon & Bromley 2005). These probability and collision arguments suggest that a single collision is an extremely unlikely explanation for the origin of the observed dust.

The polar ring model does not have these issues. The secular evolution of particles in the 99 Her system means that particles on polar orbits suffer only minor changes in inclination and node (Fig. 7). These orbits are therefore stable over the stellar lifetime, so the dust could be the steady-state collision products of the polar planetesimal belt. Initial misalignment is therefore the only special requirement for the polar ring model. The excellent agreement between the PACS data and a simple model generated by particles on these orbits argues strongly in favour of this interpretation.

The question is then shifted to one of the origin of the misalignment. Most binaries are thought to form through fragmentation and subsequent accretion during collapse of a molecular cloud (for a recent review, see Goodwin et al. 2007). The resulting binary systems should be aligned with their protoplanetary discs when the separations are of the order of tens of au (Bate et al. 2000). Given the 16-au separation of the 99 Her system, it therefore seems that interactions

[6] Had we found that an eccentric ring could explain the data, the same argument applied to ring spreading by pericentre precession would apply, with the same 1:10 result. The particles' pericentre directions are unlikely to be maintained through forcing by a third (circumbinary) body as for a standard pericentre glow model, because the perturbing body would be subject to the same pericentre precession.

during the subsequent phase of dynamical cluster evolution are a more likely cause of a misaligned disc.

There are several ways in which such a configuration could arise from interactions in a young stellar cluster. A close encounter in which a binary captures some material from the outer regions of a circumstellar disc hosted by another star seems possible. This 'disc exchange' scenario requires an encounter where the binary pericentre is perpendicular to the circumstellar disc plane, and that the encounter distance and geometry captures material into orbits similar to those observed for the debris disc (e.g. most likely a prograde rather than retrograde encounter).

An alternative scenario is a stellar exchange reaction, where a binary encounters a single star that harbours a circumstellar disc. During the exchange, one of the binary components is captured by the originally single star and the other leaves (e.g. Moeckel & Goddi 2012). The post-encounter configuration is then a binary surrounded by a circumbinary disc. If the binary pericentre direction were perpendicular to the disc plane, it could represent a young analogue of the 99 Her system. Such an encounter would require that the disc is not irreparably damaged by large stellar excursions during the exchange (Moeckel & Goddi 2012), but may also present a way to clear inner disc regions, thus providing a possible reason that the 99 Her disc resides at 120 au and not closer, where it could still be stable (see Section 5.1.1).

Both scenarios require some degree of tuning; the encounters must happen with specific geometries to produce the observed relative binary and disc orientations. However, differences in the surface brightness between the different models in Fig. 8 mean that there could be some selection bias towards more disc-like structures. The advantage of the disc exchange scenario is that the cross-section for interaction at a distance of about 100 au is much higher than that for stellar exchange, which would need to have an encounter distance similar to the binary semimajor axis. With a factor of about 10 difference in the encounter impact parameter for each scenario, the close encounter is therefore about 100 times more likely than the exchange (ignoring other constraints on geometry, configuration, etc.).

In the absence of detailed simulations of encounter outcomes, some data exist to help distinguish between these two scenarios. The minimum inclination of the stellar pole for the 99 Her primary relative to the binary orbital plane is $20^\circ \pm 10^\circ$ (Hale 1994). The inclination difference is therefore different from the binary plane with 95 per cent confidence, and is a hint that the system may be the result of an exchange. However, the scatter in inclination differences for binaries with separations similar to that of 99 Her is about 20° (Hale 1994), which may indicate that systems with this separation are in fact aligned and the uncertainties were underestimated, or that this scatter is the intrinsic level of misalignment at these separations.

Though 99 Herculis is the first clear case of misalignment between binary and disc planes, the GG Tauri system may show a similar signature. The GG Tau system consists of an Aa/Ab binary surrounded by a circumbinary ring (Guilloteau, Dutrey & Simon 1999; Piétu et al. 2011), and a more distant Ba/Bb pair that may be bound (Beust & Dutrey 2006). It is not clear if the inner binary is misaligned with the circumbinary disc, but is suggested because if they are aligned the ring's inner edge is too distant to be set by the binary (Beust & Dutrey 2005, 2006; Köhler 2011). However, there could also be problems if they are misaligned, because the expected disc scaleheight due to perturbations from the binary may be inconsistent with observations (Beust & Dutrey 2006). Though uncertain, the possible misalignment between the binary and ring planes shows that GG Tau could be a young analogue of 99 Her-like systems.

7 SUMMARY

We have modelled the resolved circumbinary debris disc in the 99 Her system. This disc is unusual because it appears misaligned with the binary plane. It can be explained as either an inclined transient ring due to a recent collision, or more likely a ring of polar orbits. The transient ring is shown to be implausible from collisional arguments. While the inclined ring cannot exist on long (secular) time-scales, the polar ring can.

There appear to be two possible formation scenarios for the polar ring model, which both invoke stellar encounters. The binary may have captured material from another stars' circumstellar disc, or a new binary may have formed in a stellar exchange where one of the systems already contained a circumstellar disc.

While many binary and multiple systems are known to have debris discs, none are resolved and have orbits characterized as well as 99 Herculis. Future efforts should characterize this system further to test our interpretation and attempt to find more examples. A sample of resolved circumbinary discs would test whether disc–binary misalignment is a common outcome of star formation and cluster evolution, with implications for planetary systems around both single and binary stars.

ACKNOWLEDGMENTS

We are grateful to the referee for a thorough reading of the manuscript, especially for noting that previous 99 Her visual orbits have the wrong ascending node. This research has made use of the Washington Double Star Catalog maintained at the U.S. Naval Observatory, and the SwiftVis *n*-body visualization software developed by Mark Lewis. We also thank Herve Beust for use of the HJS code and Paul Harvey for comments on a draft of this article.

REFERENCES

Abt H. A., Willmarth D., 2006, ApJS, 162, 207
Adelman S. J., Caliskan H., Kocer D., Cay I. H., Gokmen Tektunali H., 2000, MNRAS, 316, 514
Amblard A. et al., 2010, A&A, 518, L9
Augereau J. C., Nelson R. P., Lagrange A. M., Papaloizou J. C. B., Mouillet D., 2001, A&A, 370, 447
Bate M. R., Bonnell I. A., Clarke C. J., Lubow S. H., Ogilvie G. I., Pringle J. E., Tout C. A., 2000, MNRAS, 317, 773
Beust H., 2003, A&A, 400, 1129
Beust H., Dutrey A., 2005, A&A, 439, 585
Beust H., Dutrey A., 2006, A&A, 446, 137
Boesgaard A. M., McGrath E. J., Lambert D. L., Cunha K., 2004, ApJ, 606, 306
Churcher L. J. et al., 2011, MNRAS, 417, 1715
Dommanget J., Nys O., 2002, VizieR Online Data Catalog, 1274, 0
Doolin S., Blundell K. M., 2011, MNRAS, 418, 2656
Farago F., Laskar J., 2010, MNRAS, 401, 1189
Fruchter A. S., Hook R. N., 2002, PASP, 114, 144
Goodwin S. P., Kroupa P., Goodman A., Burkert A., 2007, Protostars and Planets V. Univ. Arizona Press, Tucson, p. 133
Gratton R. G., Carretta E., Castelli F., 1996, VizieR Online Data Catalog, 331, 40191
Griffin M. J. et al., 2010, A&A, 518, L3
Guilloteau S., Dutrey A., Simon M., 1999, A&A, 348, 570
Hale A., 1994, AJ, 107, 306
Hartkopf W. I., Mason B. D., Worley C. E., 2001, AJ, 122, 3472

Hauck B., Mermilliod M., 1997, VizieR Online Data Catalog, 2215, 0
Henry T. J., McCarthy D. W., Jr, 1993, AJ, 106, 773
Ishihara D. et al., 2010, A&A, 514, A1
Kenyon S. J., Bromley B. C., 2005, AJ, 130, 269
Koerner D. W. et al., 2010, ApJ, 710, L26
Köhler R., 2011, A&A, 530, A126
Kozai Y., 1962, AJ, 67, 591
Li A., Greenberg J. M., 1997, A&A, 323, 566
Lidov M. L., 1962, Planet. Space Sci., 9, 719
Mason B. D., Wycoff G. L., Hartkopf W. I., Douglass G. G., Worley C. E., 2011, VizieR Online Data Catalog, 1, 2026
Matthews B. C. et al., 2010, A&A, 518, L135
Mermilliod J. C., 2006, VizieR Online Data Catalog, 2168, 0
Moeckel N., Goddi C., 2012, MNRAS, 419, 1390
Moshir M. et al., 1990, *IRAS* Faint Source Catalogue, version 2.0
Nordström B. et al., 2004, A&A, 418, 989
O'Brien D. P., Greenberg R., 2003, Icarus, 164, 334
Ott S., 2010, in Mizumoto Y., Morita K. I., Ohishi M., eds, ASP Conf. Ser. Vol. 434, Astronomical Data Analysis Software and Systems XIX. Astron. Soc. Pac., San Francisco, p. 139
Perryman M. A. C., ESA, eds, 1997, The Hipparcos and Tycho Catalogues: Astrometric and Photometric Star Catalogues Derived from the ESA Hipparcos Space Astrometry Mission, ESA Special Publ. Vol. 1200. ESA, Noordwijk
Phillips N. M., Greaves J. S., Dent W. R. F., Matthews B. C., Holland W. S., Wyatt M. C., Sibthorpe B., 2010, MNRAS, 403, 1089
Piétu V., Gueth F., Hily-Blant P., Schuster K.-F., Pety J., 2011, A&A, 528, A81
Pilbratt G. L. et al., 2010, A&A, 518, L1
Poglitsch A. et al., 2010, A&A, 518, L2
Rieke G. H. et al., 2004, ApJS, 154, 25
Rieke G. H. et al., 2008, AJ, 135, 2245
Scardia M. et al., 2008, Astron. Nachr., 329, 54
Scardia M., Prieur J.-L., Pansecchi L., Argyle R. W., Sala M., 2010, Astron. Nachr., 331, 286
Söderhjelm S., 1999, A&A, 341, 121
Stewart S. T., Leinhardt Z. M., 2009, ApJ, 691, L133
Takeda Y., 2007, PASJ, 59, 335
Trilling D. E. et al., 2007, ApJ, 658, 1289
van Leeuwen F., 2008, VizieR Online Data Catalog, 1311, 0
Verrier P. E., Evans N. W., 2008, MNRAS, 390, 1377
Verrier P. E., Evans N. W., 2009, MNRAS, 394, 1721
Wiegert P. A., Holman M. J., 1997, AJ, 113, 1445
Wyatt M. C., Dent W. R. F., 2002, MNRAS, 334, 589
Wyatt M. C., Dermott S. F., Telesco C. M., Fisher R. S., Grogan K., Holmes E. K., Piña R. K., 1999, ApJ, 527, 918
Wyatt M. C., Smith R., Greaves J. S., Beichman C. A., Bryden G., Lisse C. M., 2007a, ApJ, 658, 569
Wyatt M. C., Smith R., Su K. Y. L., Rieke G. H., Greaves J. S., Beichman C. A., Bryden G., 2007b, ApJ, 663, 365

This paper has been typeset from a TEX/LATEX file prepared by the author.